PERGAMON

International Journal of Solids and Structures 39 (2002) 5205–5223

INTERNATIONAL JOURNAL OF SOLIDS and STRUCTURES

www.elsevier.com/locate/ijsolstr

Concrete in compression: a plasticity theory with a novel hardening law

Peter Grassl *, Karin Lundgren, Kent Gylltoft

Department of Structural Engineering, Concrete Structures, Chalmers University of Technology, SE-41296 Gothenburg, Sweden

Received 28 November 2001; accepted 4 July 2002

Abstract

This paper deals with the modelling of the behaviour of plain concrete in triaxial compression using the theory of plasticity. The aim is to model the load resistance and the deformation capacity in uniaxial, biaxial and triaxial compression by means of few parameters, which can be determined easily.

A novel hardening law based on a non-associated flow rule and the volumetric plastic strain as hardening parameter is combined with a yield surface proposed by Menétrey and William (1995). The novel hardening and softening law differs from a classic strain-hardening law, as instead of the length of the plastic strain vector only the volumetric component of the latter is used as a hardening parameter. Thus, the non-linearity of the plastic potential is utilized to describe the influence of multiaxial compression on the deformation capacity and no additional ductility measure is required.

The implementation and calibration of the novel hardening law are discussed. The prediction of the model is compared to results of uniaxial, biaxial and triaxial compression tests. It is shown that with one set of calibration parameters a good prediction of the load resistance and the deformation capacity for all three types of compression tests can be achieved.

Keywords: Constitutive modelling; Concrete; Compression; Triaxial stress states; Theory of plasticity; Hardening law

1. Introduction

Multiaxial stress states govern in many cases the load resistance of concrete structures. It is known that under multiaxial compression the load resistance and the deformation capacity of concrete are increased. Multiaxial compression stress states are often activated by prevented deformations. There is a strong interaction of the non-linear deformations and the activation of confining stresses. Hence, a realistic description of the deformations of concrete in triaxial compression is as important as the formulation of the strength envelope.

* Corresponding author. Tel.: +46-31-7722251; fax: +46-31-7722260.
E-mail address: peter.grassl@ste.chalmers.se (P. Grassl).

0020-7683/02/$ - see front matter © 2002 Elsevier Science Ltd. All rights reserved.
PII: S0020-7683(02)00408-0

Nomenclature

A	parameter for the plastic potential
B	parameter for the plastic potential
$\mathbf{D}^{\mathrm{e}}$	elastic stiffness matrix
$\mathbf{D}^{\mathrm{ep}}$	elastic–plastic stiffness matrix (consistent tangent modulus)
E	Young's modulus
$\mathbf{e}^{\mathrm{p}}$	deviatoric plastic strain vector
f	yield surface
f_{c}	strength of concrete in uniaxial compression
f_{t}	strength of concrete in uniaxial tension
$\mathbf{f}_{\boldsymbol{\sigma}}$	derivation of the yield surface with respect to the stress
g	plastic potential
$\mathbf{g}_{\boldsymbol{\sigma}}$	derivation of the plastic potential with respect to stress
$\mathbf{g}_{\boldsymbol{\sigma\sigma}}$	second derivation of the plastic potential with respect to stress
I_1	first invariant of the stress tensor
J_2	second invariant of the deviatoric stress tensor
J_3	third invariant of the deviatoric stress tensor
$\mathbf{Q}$	special matrix defined in Eq. (20)
$q_{\mathrm{h}}(\kappa)$	hardening function
$q_{\mathrm{s}}(\kappa)$	softening function
$\mathbf{R}$	special matrix defined in Eq. (21)
$\mathbf{r}$	backward-Euler corrector
$\delta_{ij}, \boldsymbol{\delta}$	Kronecker delta
$\varepsilon^{\mathrm{p}}_{ij}, \boldsymbol{\varepsilon}^{\mathrm{p}}$	plastic strain tensor, plastic strain vector
$\varepsilon^{\mathrm{p}}_{\mathrm{v}}$	volumetric plastic strain
κ	hardening parameter
$\dot{\lambda}, \Delta\lambda$	plastic multiplier
$\delta\lambda$	variation of the plastic multiplier
ν	Poisson's ratio
ρ	unified co-ordinate in the Haigh–Westergaard stress space
θ	co-ordinate in the Haigh–Westergaard stress space
$\sigma^{\mathrm{tr}}_{ij}, \boldsymbol{\sigma}^{\mathrm{tr}}$	trial stress tensor, trial stress vector
$\sigma_{ij}, \boldsymbol{\sigma}$	stress tensor, stress vector
$\boldsymbol{\delta\sigma}$	variation of the stress vector
ξ	unified co-ordinate in the Haigh–Westergaard stress space
ψ	inclination of the plastic strain

Both biaxial and triaxial compressive stress states occur in existing concrete structures. Often it is not possible to exclude one of these stress states a priori, e.g. due to cracking during the loading process. The load resistance and the deformation capacity increase for both biaxial and triaxial compression stress states. In the triaxial case, however, the increase is very significant. Consequently, it is required that a model can describe the load resistance and the deformation capacity of the material both in mainly biaxial and in triaxial stress states.

In the present study, the theory of plasticity is used to model the behaviour of plain concrete subjected to multiaxial compressive loading. The behaviour of concrete in compression is characterized by inelastic

deformations. Therefore, the split of strains into elastic and plastic parts within the theory of plasticity is of advantage. The evolution of the plastic part of the strains is determined by the gradient of the plastic potential.

Hardening and softening of the material can be described by means of the change of the size and location of the yield surface, which is controlled by the hardening parameter. Commonly, the length of the plastic strain vector is used as hardening parameter, i.e. to control the size of the yield surface.

However, this hardening parameter is not suitable to describe the increase of plastic deformations in multiaxial compression stress states. Therefore, formulations in which the hardening parameter is a scaled form of the length of the plastic strain, depending on the stress states, were introduced in the literature. Scaling functions based on the hydrostatic pressure were introduced by Etse and Willam (1994), Malvar et al. (1997) and Menétrey (1994). The major principal stress component was utilized, for example, by Pivonka et al. (2000). A hardening function depending on the intermediate principal stress component was introduced by Barros (2001). Johansson and Åkesson (2002) used the mean of the two major principal stresses to describe the influence of confinement on both strength and deformation behaviour.

In the novel hardening law proposed in this study, the influence of multiaxial stress states on the deformation capacity is achieved by introducing a modified strain-hardening parameter. Instead of the length of the plastic strain vector, the volumetric part of the latter is used. Or in terms of the theory of invariants, instead of the second invariant, the first invariant of the plastic strain tensor is used. In combination with a non-linear plastic potential the deformation capacity in multiaxial compression can be described. This hardening law is combined with a yield surface based on the Hoek and Brown failure criterion, which represents the strength in both triaxial and biaxial compression stress states. Consequently, it is expected to be able to model the load resistance and the deformation capacity in uniaxial, biaxial and triaxial compression by means of one calibration.

2. Constitutive modelling

The plasticity theory proposed in this study consists of a novel hardening law, which describes the deformation capacity in multiaxial compression, combined with a yield surface proposed by Menétrey and Willam (1995). Both the plastic potential within the hardening law, and the yield surface, are constituted by using the unified co-ordinates in the Haigh–Westergaard stress space (see e.g. Chen and Han (1988)) which are based on the stress invariants.

The three unified co-ordinates ξ, ρ and θ are defined as

$$\xi = \frac{I_1}{\sqrt{3} f_c}, \qquad I_1 = \delta_{ij}\sigma_{ij}, \qquad \delta_{ij} = 1, \quad \text{if } i = j \quad \text{and} \quad \delta_{ij} = 0, \quad \text{if } i \neq j, \tag{1}$$

$$\rho = \frac{\sqrt{2J_2}}{f_c}, \qquad J_2 = \frac{1}{2} s_{ij} s_{ij}, \qquad s_{ij} = \sigma_{ij} - \frac{1}{3}\delta_{ij}\sigma_{kk}, \tag{2}$$

$$\cos 3\theta = \frac{3\sqrt{3}}{2} \frac{J_3}{J_2^{3/2}}, \qquad J_3 = \frac{1}{3} s_{ij} s_{jk} s_{ki}. \tag{3}$$

The geometrical interpretation is shown in Fig. 1.

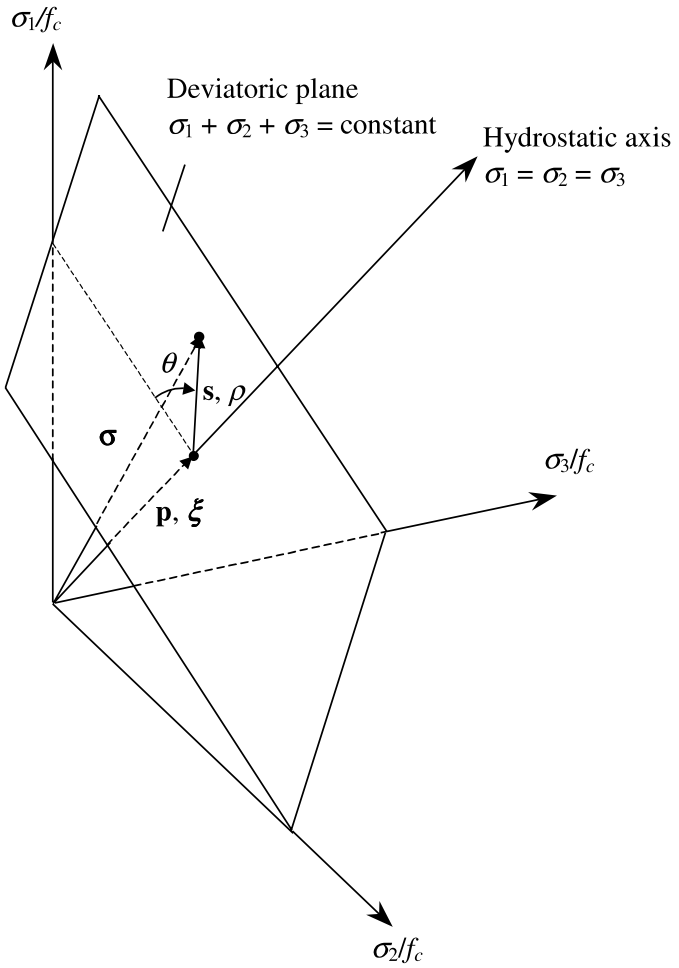

Fig. 1. Haigh–Westergaard stress space.

2.1. Yield surface

A three-parameter yield surface, which depends on three stress invariants and all principal stress components, is used. It is an extension of the Hoek and Brown failure criterion and was proposed by Menétrey and Willam (1995). It has the form

$$f = (\sqrt{1.5}\rho)^2 + q_h(\kappa)m\left[\frac{\rho}{\sqrt{6}}r(\theta, e) + \frac{\xi}{\sqrt{3}}\right] - q_h(\kappa)q_s(\kappa) \leqslant 0, \tag{4}$$

where m is defined as

$$m = 3\frac{f_c^2 - f_t^2}{f_c f_t}\frac{e}{e+1} \tag{5}$$

and the elliptic function as

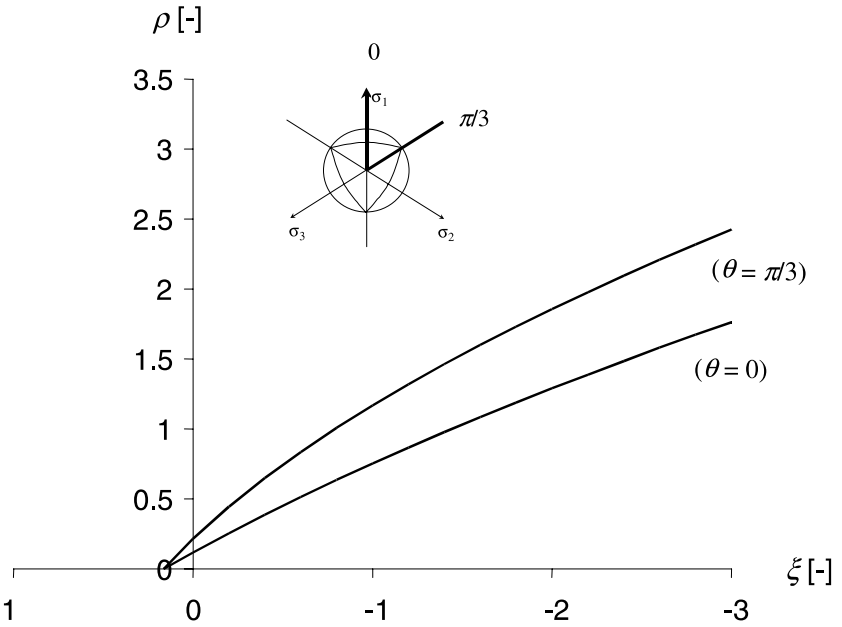

Fig. 2. The yield surface in the ρ'–ξ' plane. The compressive meridian at $\theta = \pi/3$ and the tensile $\theta = 0$ are presented.

$$r(\theta, e) = \frac{4(1-e^2)\cos^2\theta + (2e-1)^2}{2(1-e^2)\cos\theta + (2e-1)[4(1-e^2)\cos^2\theta + 5e^2 - 4e]^{1/2}}. \tag{6}$$

The elliptic function $r(\theta, e)$ describes the out-of-roundness of the deviatoric section and is controlled by the eccentricity e. The three calibration parameters are the strength in uniaxial compression f_c, the strength in uniaxial tension f_t and the eccentricity e. The calibration of the eccentricity e is illustrated in Section 4.

The surface possesses parabolic meridians, as shown in Fig. 2, and the deviatoric sections change from triangular shapes at low confinement to almost circular shapes at high confinement, as shown in Fig. 3. In this way the change from quasi-brittle to ductile behaviour with increasing hydrostatic pressure can be described. The surface is smooth and convex, except the point of equitriaxial tension, where the parabolic meridians intersect the hydrostatic axis.

2.2. Novel hardening law and non-associated flow rule

The novel hardening law presented in this study describes the influence of multiaxial stress states on the deformation capacity. This is achieved by combining the volumetric plastic strain as hardening parameter with a non-linear plastic potential.

The evolution of the plastic strain rate is determined by the flow rule

$$\dot{\varepsilon}^{\mathrm{p}}_{ij} = \dot{\lambda}\frac{\partial g}{\partial \sigma_{ij}}. \tag{7}$$

The flow rule is non-associated, meaning that the form of the plastic potential differs from the form of the yield surface. It has a quadratic form and is constituted, using the co-ordinates in the Haigh–Westergaard stress space, as

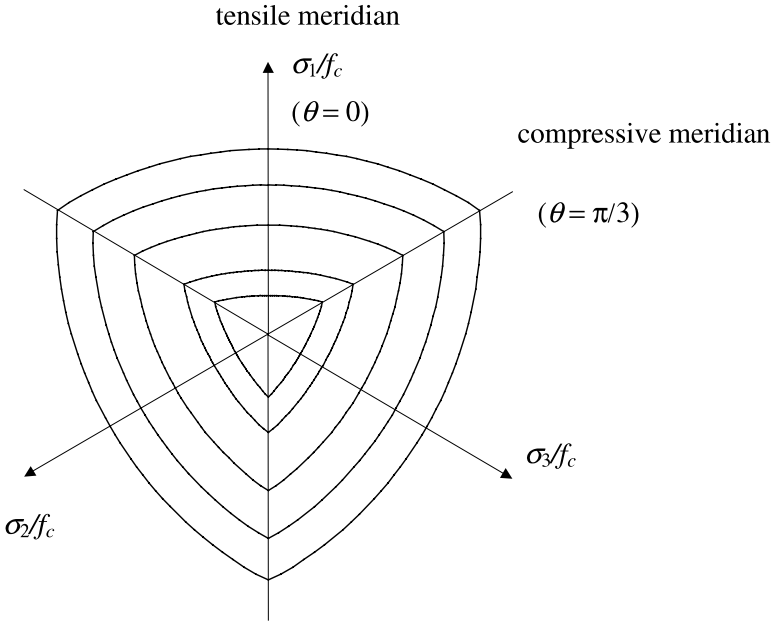

Fig. 3. The shape of the yield surface in the deviatoric plane for different hydrostatic stresses.

$$g = -A\left(\frac{\rho}{\sqrt{q(\kappa)}}\right)^2 - B\frac{\rho}{\sqrt{q(\kappa)}} + \frac{\xi}{\sqrt{q(\kappa)}} = 0. \tag{8}$$

The two parameters A and B are determined by means of the axial strain at maximum stress in uniaxial compression and in a triaxial compressive state. The determination is described in detail in Section 4.

The hardening parameter is the volumetric component of the plastic strain increment:

$$\dot{\kappa}(\dot{\varepsilon}^{\mathrm{p}}) = \dot{\varepsilon}_v^{\mathrm{p}} = \delta_{ij}\dot{\varepsilon}_{ij}^{\mathrm{p}} = \dot{\lambda}\delta_{ij}\frac{\partial g}{\partial \sigma_{ij}} = \dot{\lambda}\frac{\sqrt{3}}{\sqrt{q(\kappa)}f_{\mathrm{c}}}, \tag{9}$$

where δ_{ij} is the Kronecker delta, defined in the third term of Eq. (1). Thus, the hardening parameter depends entirely on the plastic strain. This is one of the main differences from other plasticity theories in which the hardening variable depends on the plastic strain and the stress state, as discussed in Section 1.

The hardening/softening law has the form $q(\kappa) = (\sigma_{\mathrm{c}}(\kappa)/f_{\mathrm{c}})^2$, where σ_{c} is the stress in uniaxial compression and κ the hardening parameter, which is the volumetric component of the corresponding plastic strain vector. The cohesive strength and the friction parameter m, within the formulation of the yield surface in Eq. (4), are uncoupled so that they can be adjusted separately to control hardening and softening. Therefore, the hardening/softening function $q(\kappa)$ is split up into one function concerning the hardening, $q_{\mathrm{h}}(\kappa)$, and one concerning the softening, $q_{\mathrm{s}}(\kappa)$:

$$q(\kappa) = q_{\mathrm{h}}(\kappa)q_{\mathrm{s}}(\kappa), \tag{10}$$

as shown in Fig. 4. By means of the split, residual strength in multiaxial compression is provided, as illustrated in Figs. 5 and 6.

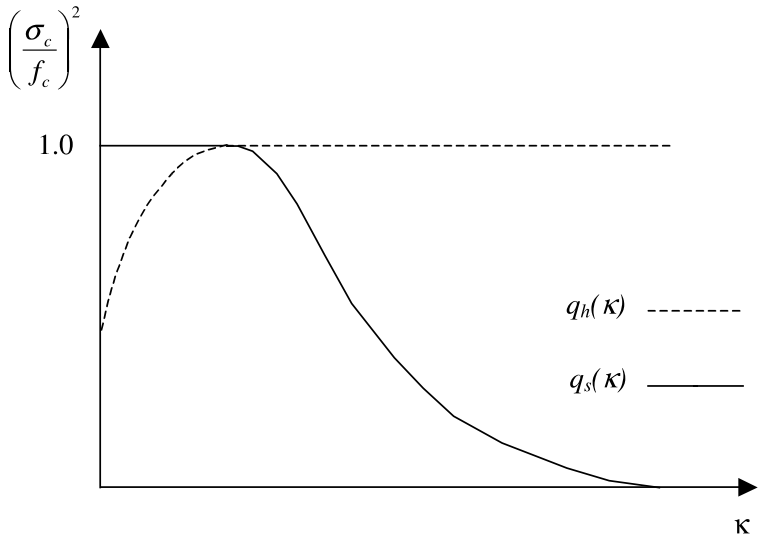

Fig. 4. Split of the hardening function into a hardening and softening part.

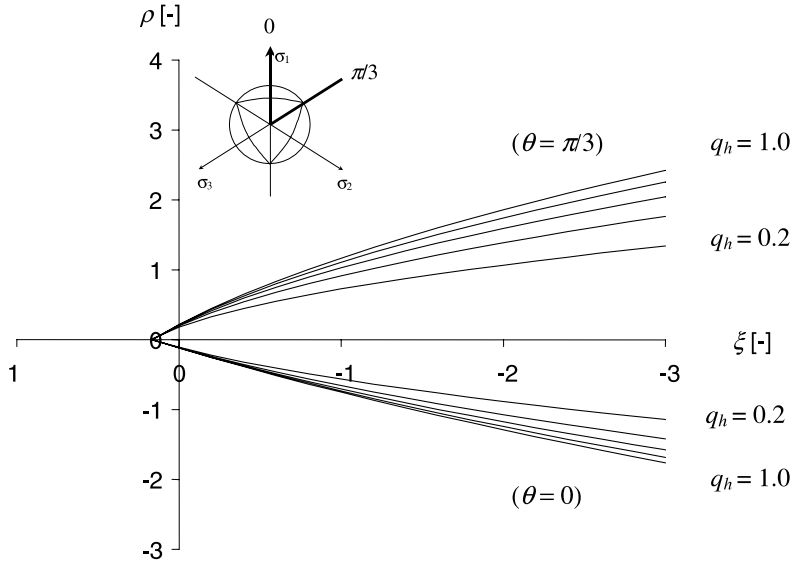

Fig. 5. Evolution of the compressive meridian ($\theta = \pi/3$) and the tensile meridian ($\theta = 0$) of the yield surface in hardening.

The plastic potential in Eq. (8) describes the deformation capacity of plain concrete in multiaxial compression. For dominant tensile loading ($\sigma_1 + \sigma_2 + \sigma_3 > 0$), however, the deformation capacity cannot be described accurately with the chosen plastic potential. Even though the proposed theory is focused on compression loading, the novel hardening parameter can also be used to describe concrete in tension, if a more enhanced form of plastic potential is chosen.

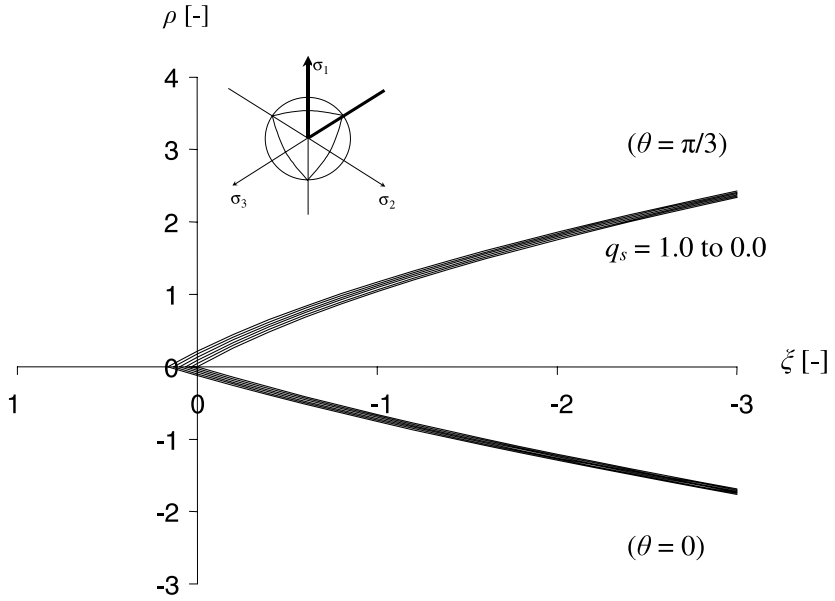

Fig. 6. Evolution of the compressive meridian ($\theta = \pi/3$) and the tensile meridian ($\theta = 0$) of the yield surface in softening.

3. Numerical implementation

A backward-Euler algorithm is applied for the constitutive integration and combined with a tangent modulus, which is consistent with the algorithm. The algorithm was studied in detail by Zeng et al. (1996). The backward-Euler algorithm is based on the operator split technique, which was introduced by Simo and Ortiz (1985). The consistent tangent modulus was introduced by Simo and Taylor (1985).

The algorithm for each integration point for a given strain state can be summarized by means of the following steps:

(1) Compute the trial stress

$$\boldsymbol{\sigma}^{\mathrm{tr}} = \mathbf{D}^{\mathrm{e}}(\boldsymbol{\varepsilon} - \boldsymbol{\varepsilon}^{\mathrm{p}}_{n-1}). \tag{11}$$

(2) Control the yield condition

$$f = f(\boldsymbol{\sigma}^{\mathrm{tr}}, q_{n-1}). \tag{12}$$

If $f \geqslant 0$, go to (3)

$$\boldsymbol{\sigma} = \boldsymbol{\sigma}^{\mathrm{tr}}, \tag{13}$$

$$\mathbf{D}^{\mathrm{ep}} = \mathbf{D}^{\mathrm{e}}. \tag{14}$$

(3) Initial return:

$$H(\kappa) = \frac{\partial f}{\partial q}\frac{\partial q}{\partial \kappa}\boldsymbol{\delta}^{\mathrm{T}}\mathbf{g}_{\boldsymbol{\sigma}}, \tag{15}$$

$$\Delta\lambda = \frac{f(\boldsymbol{\sigma}^{\mathrm{tr}})}{\mathbf{f}_{\boldsymbol{\sigma}}\mathbf{D}^{\mathrm{e}}\mathbf{g}_{\boldsymbol{\sigma}} - H(\kappa)}, \tag{16}$$

$$\boldsymbol{\sigma}_n = \boldsymbol{\sigma}^{\mathrm{tr}} - \Delta\lambda \mathbf{D}^{\mathrm{e}} \mathbf{g}_{\boldsymbol{\sigma}}. \tag{17}$$

(4) Iterative return:

(4.1) Control yield condition and compute the backward-Euler corrector

$$f = f(\boldsymbol{\sigma}_n, q_{n-1}), \tag{18}$$

$$\mathbf{r} = \boldsymbol{\sigma} - (\boldsymbol{\sigma}^{\mathrm{tr}} - \Delta\lambda \mathbf{D}^{\mathrm{e}} \mathbf{g}_{\boldsymbol{\sigma}}), \tag{19}$$

$$\mathbf{Q} = \mathbf{I} + \Delta\lambda \mathbf{D}^{\mathrm{e}} \mathbf{g}_{\boldsymbol{\sigma}\boldsymbol{\sigma}}, \tag{20}$$

$$\mathbf{R} = \mathbf{Q}^{-1} \mathbf{D}^{\mathrm{e}}. \tag{21}$$

(4.2) Control the convergence. If $|r| \leqslant 10^{-10}$ and $f \leqslant 10^{-10}$, go to (5)

(4.3) Further return is required:

$$H(\kappa) = \frac{\partial f}{\partial q} \frac{\partial q}{\partial \kappa} \boldsymbol{\delta}^{\mathrm{T}} \mathbf{g}_{\boldsymbol{\sigma}}, \tag{22}$$

$$\delta\lambda = \frac{f(\boldsymbol{\sigma}) - \mathbf{f}_{\boldsymbol{\sigma}} \mathbf{Q}^{-1} \mathbf{r}}{\mathbf{f}_{\boldsymbol{\sigma}}^{\mathrm{T}} \mathbf{R} \mathbf{g}_{\boldsymbol{\sigma}} - H(\kappa)}, \tag{23}$$

$$\boldsymbol{\delta\sigma} = -\mathbf{Q}^{-1} \mathbf{r} - \delta\lambda \mathbf{R} \mathbf{g}_{\boldsymbol{\sigma}}. \tag{24}$$

(4.4) Return to (4.1)

(5) Update the state variables $\boldsymbol{\varepsilon}^{\mathrm{p}}$ and κ

(6) Compute the consistent tangent modular matrix $\mathbf{D}^{\mathrm{ep}}$

$$\mathbf{D}^{\mathrm{ep}} = \mathbf{R}\left(\mathbf{I} - \frac{\mathbf{g}_{\boldsymbol{\sigma}} \mathbf{f}_{\boldsymbol{\sigma}} \mathbf{R}}{\mathbf{f}_{\boldsymbol{\sigma}} \mathbf{R} \mathbf{g}_{\boldsymbol{\sigma}} - H(\kappa)}\right). \tag{25}$$

4. Calibration

One aim of the combination of the novel hardening law with the non-linearity of the plastic potential is to reduce the number of material parameters needed to calibrate the constitutive model. This combination is based on the following hypotheses:

I. The maximum stress in uniaxial compression, f_{c}, is reached when the volumetric strain, ε_{v}, is equal to zero, as illustrated in Fig. 7.
II. The volumetric plastic strain at maximum stress in uniaxial compression is the value of the hardening parameter when the maximum stress is reached, and is also used for all other stress states.
III. The inclination of the total plastic strain is equal to the gradient of the plastic potential within the same state of loading (see Fig. 8).

Hypothesis I is supported by experimental observations reported by Kupfer et al. (1969), van Mier (1986) and Imran (1994). Here, the load resistance in uniaxial compression was obtained at minimum volume, when the volumetric strain becomes equal to zero. However, the experimental results are dependent on boundary conditions, measurement techniques and the material composition.

Hypothesis II is very fundamental within the proposed theory. Experimental results regarding the lateral deformation capacity of confined specimens show a wide scatter. However, experimental results reported by

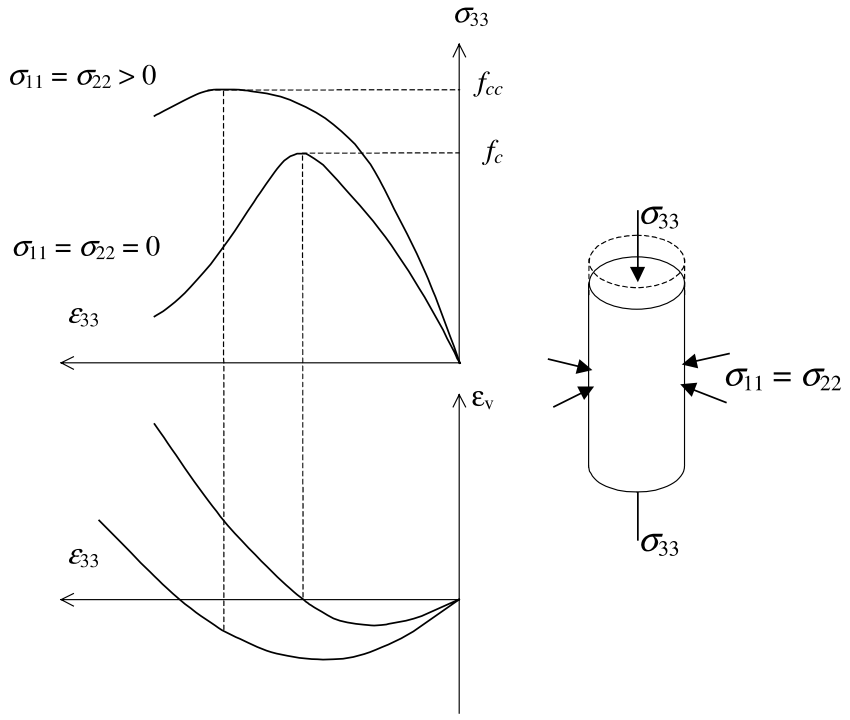

Fig. 7. Axial strain versus axial stress and volumetric strain for concrete in uniaxial and triaxial compression.

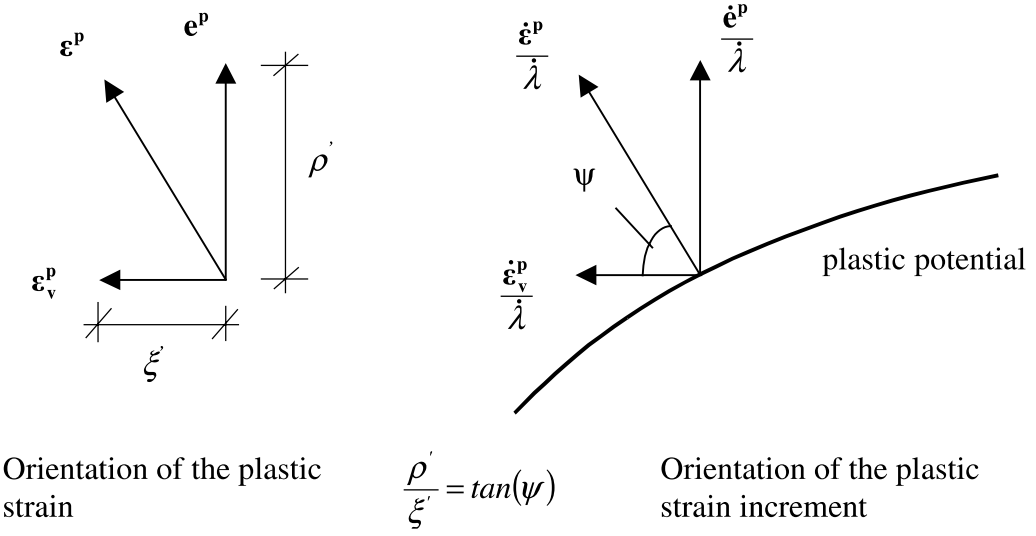

Fig. 8. Split of the plastic strain vector into a deviatoric part and a volumetric part. The direction of the plastic strain is equal to the inclination of the plastic strain increment (see hypothesis III).

Imran (1994), Smith (1985) and Kotsovos and Newman (1980) show that, with increasing confinement, the inelastic deformation capacity in axial and lateral directions is increased (see also Figs. 14 and 18).

The inclination of the plastic strain increments during monotonic loading was studied by Smith (1985). Even though a change of inclination at the beginning of monotonic loading was observed, hypothesis III seems to be generally valid. Without hypothesis III, this change of the inclination of the volumetric plastic strain might be described. However, if the inclination changes, the two parameters A and B of the plastic potential must be determined by means of the integral of the plastic flow, which complicates the calibration. However, the agreement of the model prediction with experimental results (see Section 5) might be improved.

The two parameters A and B of the plastic potential are determined by means of the axial strain in uniaxial compression at maximum stress and the axial strain in triaxial compression at maximum stress, as illustrated in Fig. 7.

The calibration is carried out in the following steps:

1. The plastic strain states for the uniaxial stress state and the triaxial stress state are calculated.

(a) Uniaxial plastic strain state

The axial plastic strain component is equal to the axial total strain component minus the elastic part:

$$\varepsilon_{33}^{\mathrm{p}} = \varepsilon_{33} - \left(-\frac{f_{\mathrm{c}}}{E} \right) \tag{26}$$

and the lateral plastic strain is determined as

$$\varepsilon_{11}^{\mathrm{p}} = \varepsilon_{22}^{\mathrm{p}} = -\frac{1}{2}\varepsilon_{33} - v\frac{f_{\mathrm{c}}}{E}. \tag{27}$$

The volumetric plastic strain is thus equal to the elastic volumetric strain; i.e. the volumetric strain equals zero.

$$\varepsilon_{\mathrm{v}}^{\mathrm{p}} = \varepsilon_{11}^{\mathrm{p}} + \varepsilon_{22}^{\mathrm{p}} + \varepsilon_{33}^{\mathrm{p}} = \frac{f_{\mathrm{c}}}{E}(1 - 2v). \tag{28}$$

(b) Triaxial plastic strain state

The axial component results as

$$\varepsilon_{33}^{\mathrm{p}} = \varepsilon_{33} - \frac{1}{E}(\sigma_{33} - v(\sigma_{11} + \sigma_{22})) \tag{29}$$

and the lateral component as

$$\varepsilon_{11}^{\mathrm{p}} = \varepsilon_{22}^{\mathrm{p}} = \frac{\varepsilon_{\mathrm{v}}^{\mathrm{p}} - \varepsilon_{33}^{\mathrm{p}}}{2}. \tag{30}$$

2. By means of the plastic strain states in uniaxial and triaxial compression, the inclinations ψ_1 and ψ_2 (see Figs. 8 and 9) can be determined to be

$$\psi = \frac{\sqrt{2}(\varepsilon_{33}^{\mathrm{p}} - \varepsilon_{11}^{\mathrm{p}})}{\varepsilon_{\mathrm{v}}^{\mathrm{p}}} \tag{31}$$

for the plastic strain state in uniaxial compression and triaxial compression.

3. The unified length of the deviatoric stress vector is determined as

$$\rho_1 = \sqrt{\frac{2}{3}} \tag{32}$$

for uniaxial compression, and

$$\rho_2 = \sqrt{\frac{2}{3}}\frac{(\sigma_{11} - \sigma_{33})}{f_{\mathrm{c}}} \tag{33}$$

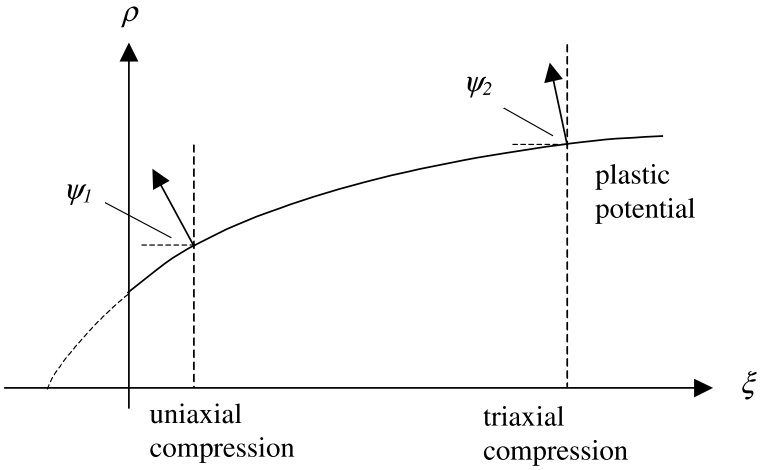

Fig. 9. Change of the inclination of the plastic strain increment along the compressive meridian, depending on the hydrostatic stress state.

for triaxial compression.

4. The derivation of the plastic potential in Eq. (8) with respect to the unified deviatoric lengths ρ_1 and ρ_2 is given by the inclinations ψ_1 and ψ_2 in Eq. (31) as

$$\frac{\partial g(\rho,\xi)}{\partial \rho} = -2A\rho - B = \psi.$$

Thus, the two parameters for the plastic potential are determined as

$$A = \frac{(\psi_2 - \psi_1)}{2(\rho_1 - \rho_2)} \tag{34}$$

and

$$B = \rho_1 \frac{(\psi_1 - \psi_2)}{\rho_1 - \rho_2} - \psi_1. \tag{35}$$

In addition to the two parameters of the plastic potential, we require the Young modulus, E, the Poisson ratio, ν, the stress–strain curve in uniaxial compression, the uniaxial compressive strength, f_c, the uniaxial tensile strength, f_t and the eccentricity e. The last-named parameter determines the ratio of uniaxial and equibiaxial compressive strengths, and depends on the ratio of uniaxial compressive strength to uniaxial tensile strength f_c/f_t, as illustrated in Fig. 10.

5. Comparison with experimental results

The response of the constitutive model is compared to experimental results from uniaxial, biaxial and triaxial compression tests. In Figs. 11–13 the yield surface at ultimate stress is compared to experimental results reported by Kupfer et al. (1969), Mills and Zimmerman (1970), Linse and Aschl (1976), Smith (1985), Scholz et al. (1995) and Imran (1994). Here, the comparison is made in the deviatoric plane, the ρ–ξ plane and the σ_1–σ_2 plane, illustrating the representation for biaxial stress states. For the calibration of the

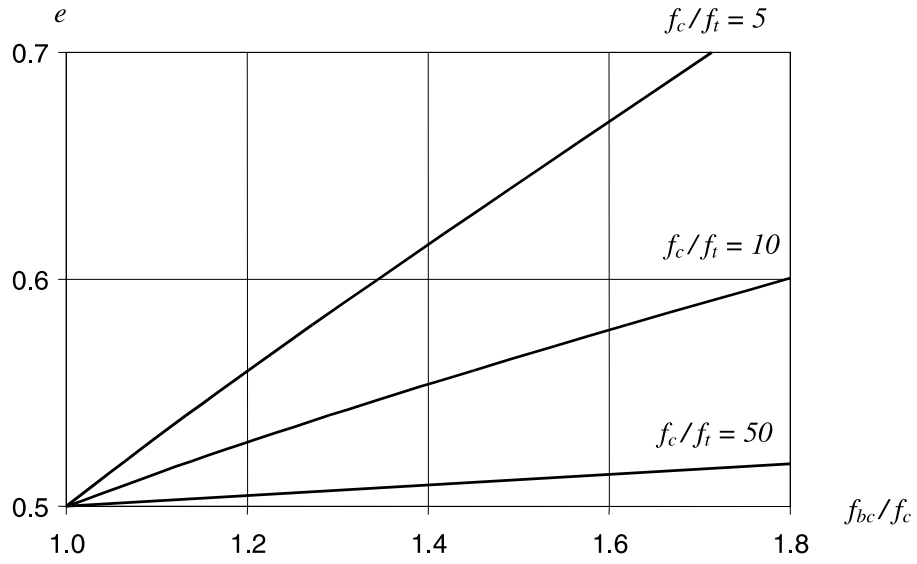

Fig. 10. Relation of the eccentricity parameter e to the biaxial strength f_{bc}. As input, the ratio of the strengths in uniaxial compression and uniaxial tension, f_c/f_t, is required.

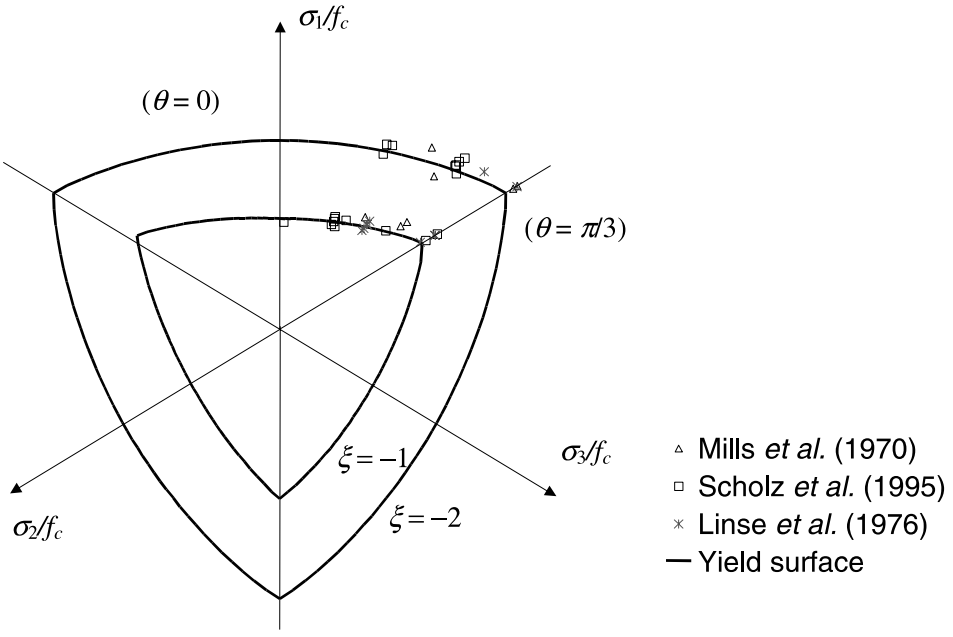

Fig. 11. Comparison of the yield condition at maximum stress to experimental results in the deviatoric plane.

yield surface, the ratio of the strengths in uniaxial compression and uniaxial tension was set to $f_c/f_t = 10$ and the ratio of equibiaxial compression to uniaxial compression to $f_{bc}/f_c = 1.16$, which corresponds to an eccentricity parameter of $e = 0.52$.

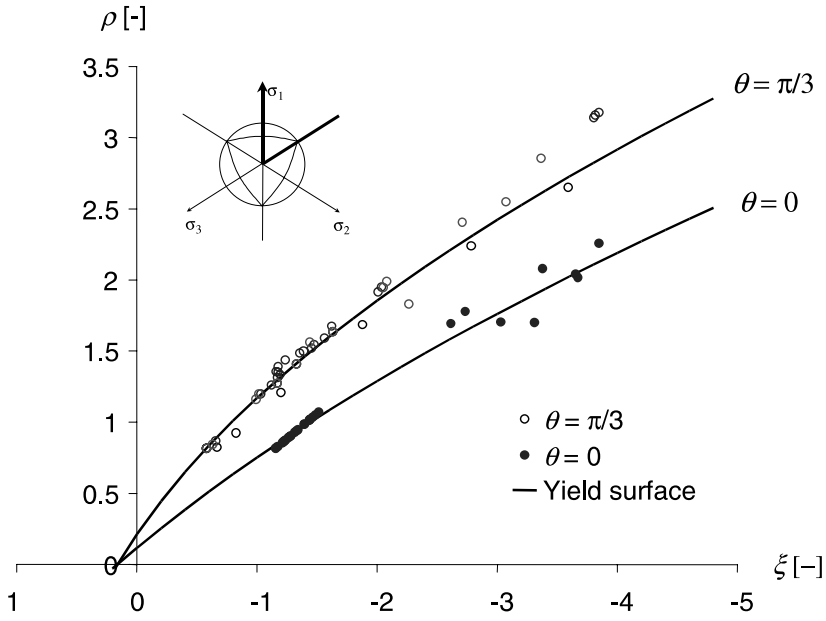

Fig. 12. Comparison of the yield condition in the ρ–ξ plane to experimental results reported by Smith (1985), Mills and Zimmerman (1970), Scholz et al. (1995), Linse and Aschl (1976) and Imran (1994).

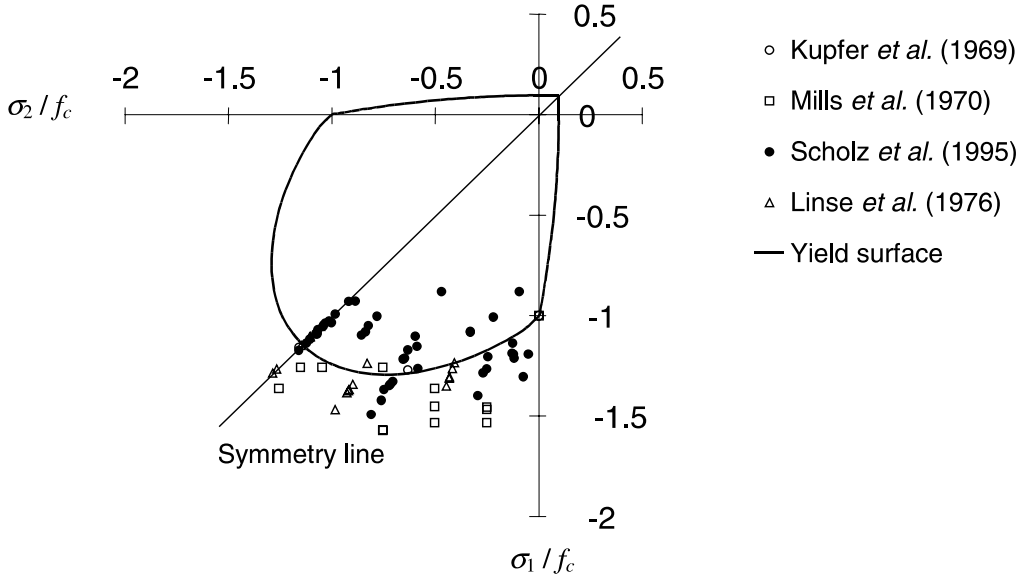

Fig. 13. Comparison of the yield criterion to experimental results in the σ_1–σ_2 plane.

Furthermore, the representation of the constitutive model was compared to multiaxial stress–strain relations from experiments reported by Imran (1994) as shown in Fig. 14. The parameters of the model were set to $A = 21.22$, $B = -31.46$, $E = 30$ GPa, $\nu = 0.15$, $f_c = 47.4$ MPa, $f_t = 4.74$ MPa and $e = 0.52$. Here, the

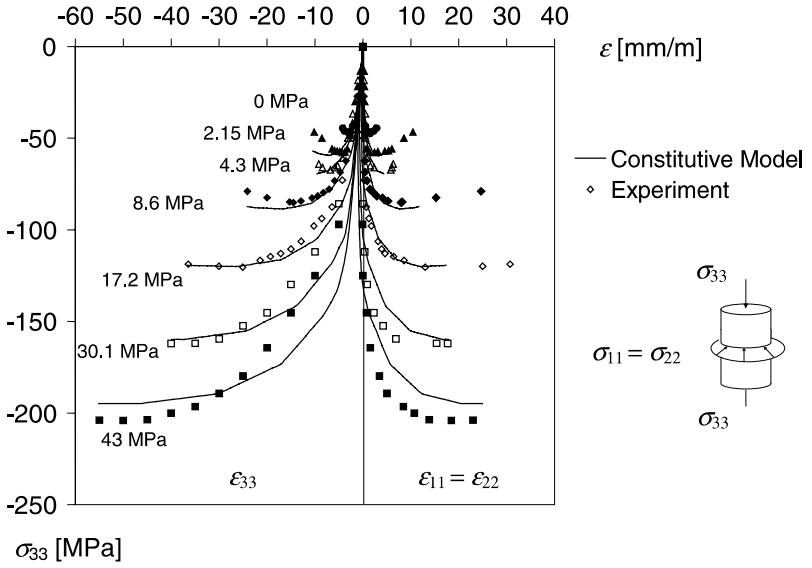

Fig. 14. Triaxial compression tests from Imran (1994) compared to the constitutive model. (Seven confinement levels from 0 to 43 MPa are shown.)

two parameters of the plastic potential (A and B) were calibrated by means of the axial strain in uniaxial compression and multiaxial compression with a lateral confinement of $\sigma_{11} = \sigma_{22} = 8.6$ MPa.

One of the key issues in this study is the representation of the behaviour of concrete in uniaxial, biaxial and triaxial compression with a single calibration. Therefore, the response of the constitutive model was compared to biaxial compression tests reported by Kupfer et al. (1969) by means of the same set of pa-

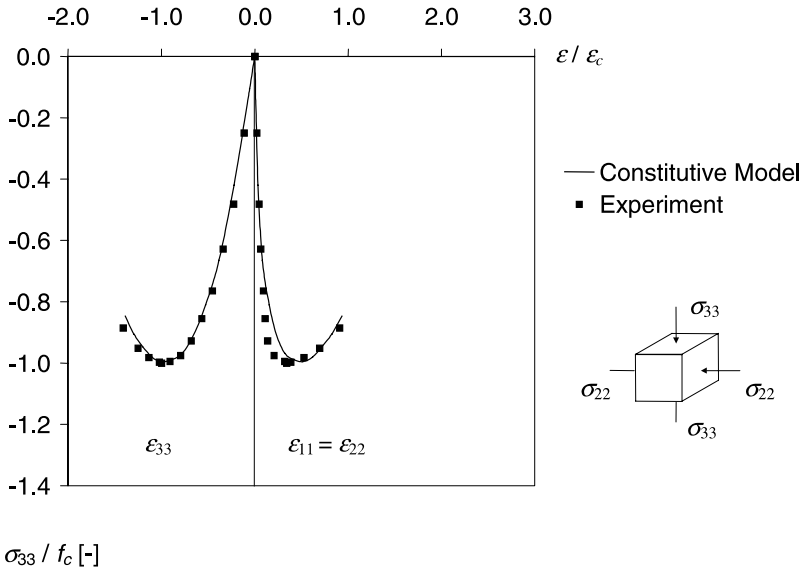

Fig. 15. Uniaxial compression tests ($\sigma_{11}/\sigma_{22} = 1.0/0.0$) reported by Kupfer et al. (1969) compared to the model prediction.

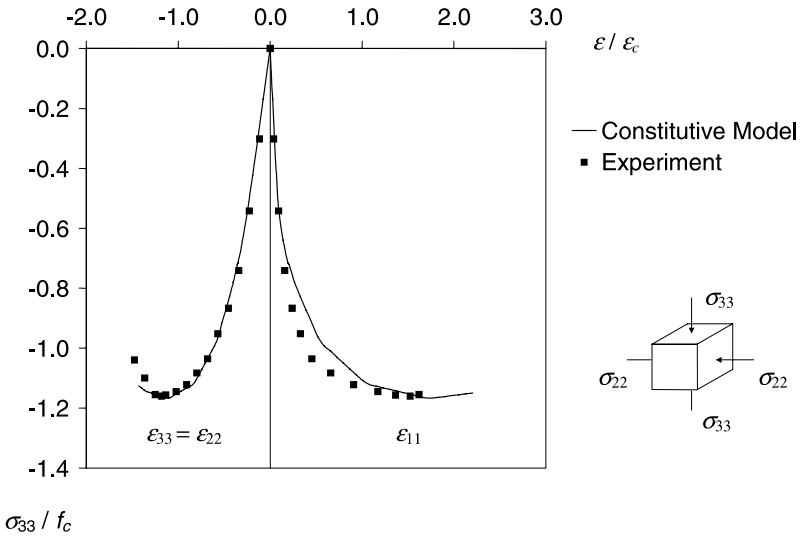

Fig. 16. Equibiaxial compression tests ($\sigma_{11}/\sigma_{22} = 1.0/1.0$) reported by Kupfer et al. (1969) compared to the model prediction.

rameters as used for the triaxial compression tests reported by Imran (1994). The results had to be unified because of the different types of concrete used in the two test series. They are shown in Figs. 15–17.

Additionally, results of triaxial compression tests reported by Kotsovos and Newman (1980) were compared to the prediction of the model in Fig. 18. The model parameters were set to $A = 15.84$, $B = -23.34$, $E = 30$ MPa, $v = 0.15$, $f_c = 46.9$ MPa, $f_t = 4.69$ MPa and $e = 0.52$. The two parameters of the plastic potential were determined by means of the axial strain at maximum stress in uniaxial compression, which was assumed to be 2.5 per mille, and the axial strain at a confinement level of 18 MPa.

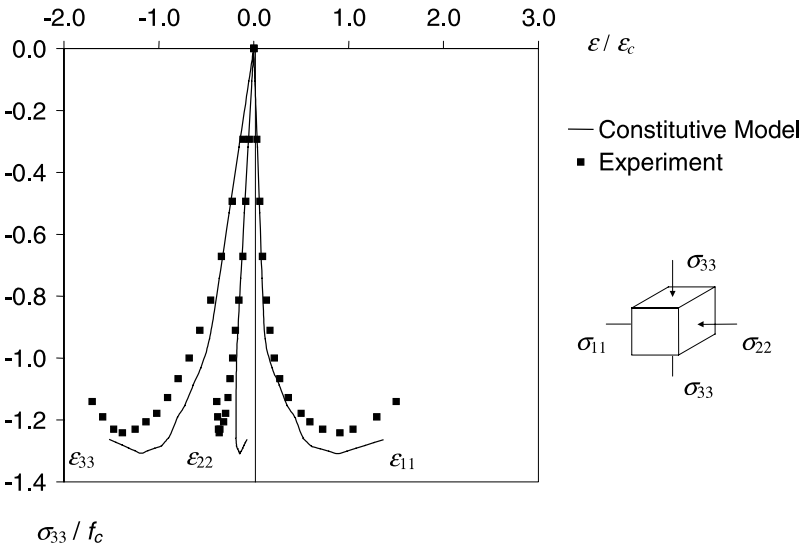

Fig. 17. Biaxial compression test ($\sigma_{11}/\sigma_{22} = 1.0/0.5$) reported by Kupfer et al. (1969) compared to the model prediction.

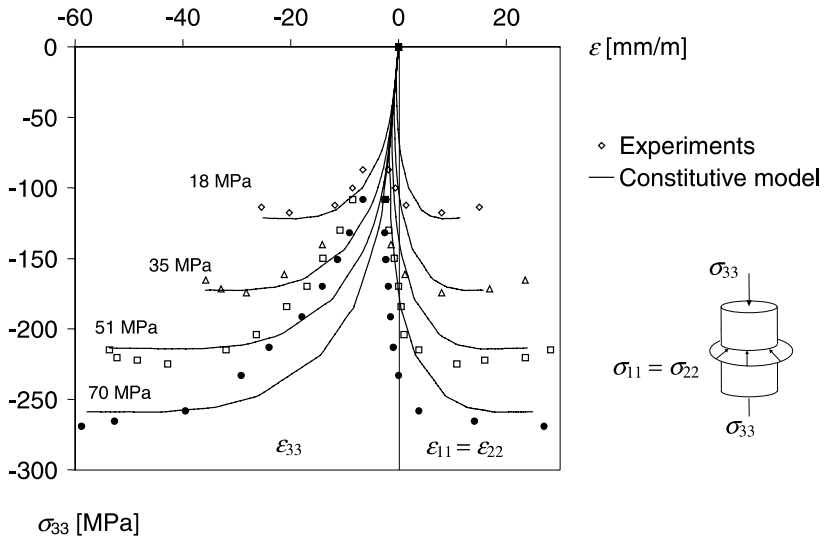

Fig. 18. Results from triaxial compression tests reported by Kotsovos and Newman (1980) compared to the prediction of the constitutive model.

Finally, results from experiments obtained at the US Army Engineers Waterways Experiment Station (USAE-WES) and reported by Bažant et al. (1996) were compared to the model prediction, as shown in Fig. 19. In these experiments, concrete cylinders were subjected to high confining lateral stresses up to a magnitude of 400 MPa. The model parameters were calibrated to $A = 13.73$, $B = -17.38$, $E = 35$ MPa, $v = 0.18$, $f_c = 45.5$ MPa, $f_t = 4.55$ MPa and $e = 0.52$. The two parameters of the plastic potential were determined by means of the axial strain at maximum stress in uniaxial compression, and the axial strain at a confinement of 20 MPa.

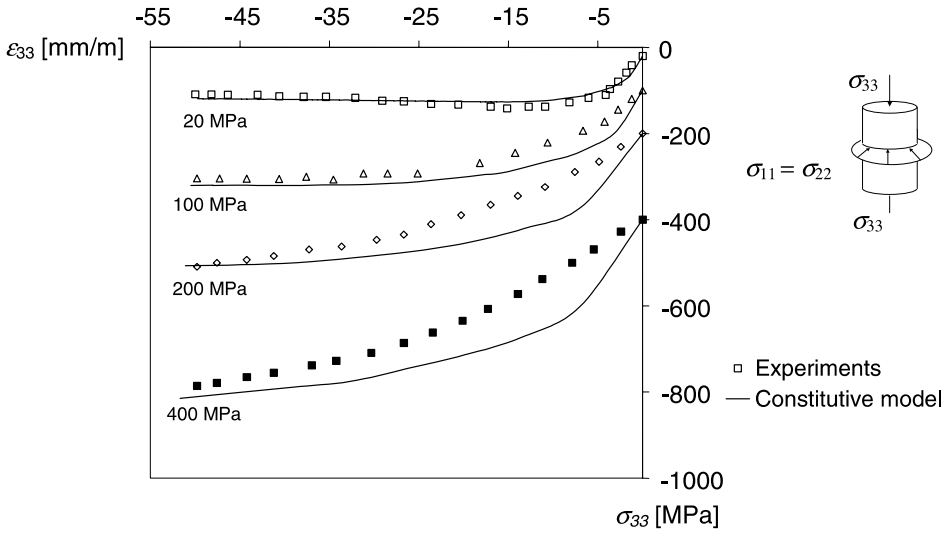

Fig. 19. Triaxial compression tests (USAE-WES, taken from Bažant et al. (1996)) compared to the model prediction.

As can be seen in Figs. 11–19, the results of the constitutive model concerning the prediction of both strength and deformations are in good agreement with the experimental results.

6. Conclusion

A plasticity theory to describe the behaviour of plain concrete in multiaxial compression is proposed. The model predicts the load resistance and the deformation capacity of plain concrete in uniaxial, biaxial and triaxial compression by means of one calibration.

The novel hardening law is based on the volumetric plastic strain as hardening parameter. In combination with a non-linear plastic potential, the increase in the deformation capacity due to multiaxial compression can be described. For the calibration of the plastic potential only two parameters are required, as no additional scaling or confinement function is needed.

The hardening law was combined with an extension of the Hoek and Brown failure criterion and implemented by means of an implicit backward-Euler algorithm. It is shown that the formulation is simplified by using the volumetric plastic strain as the hardening parameter.

Uniaxial, biaxial and triaxial compression tests are reproduced by means of the model. Experimental results for strength and deformation behaviour were found to be in good agreement with the model prediction.

The phenomenon of localization of deformations in multiaxial compression as reported by van Mier (1986) is not considered in this theory. However, a combination of the hardening law with the fracture energy of concrete in compression seems promising and will be pursued in further studies.

References

Barros, M., 2001. Elasto-plastic modelling of confined concrete elements following MC90 equations. Engineering Structures 23, 311–318.

Bažant, Z.P., Xiang, Y., Adley, M.D., Prat, P.C., Akers, S.A., 1996. Microplane model for concrete. II: Data delocalization and verification. Journal of Engineering Mechanics 122 (3), 255–262.

Chen, W.F., Han, D.J., 1988. Plasticity for Structural Engineers. Springer-Verlag Inc., New York.

Etse, G., Willam, K.J., 1994. Fracture energy formulation for inelastic behavior of plain concrete. Journal of Engineering Mechanics, ASCE 120 (9), 183–2011.

Imran, I., 1994. Applications of non-associated plasticity in modelling the mechanical response of concrete. Ph.D. Thesis, Department of Civil Engineering, University of Toronto, Canada, 208pp.

Johansson, M., Åkesson, M., 2002. Finite element study on concrete-filled steel tubes using a new confinement sensitive concrete compression model. Nordic Concrete Research 27, 43–62.

Kotsovos, M.D., Newman, J.B., 1980. Mathematical description of deformational behavior of concrete under generalized stress beyond ultimate strength. Journal of the American Concrete Institute—ACI 77 (5), 340–346.

Kupfer, H., Hilsdorf, H.K., Rusch, H., 1969. Behavior of concrete under biaxial stresses. ACI Journal, title no. 66-52, pp. 656–666.

Linse, D., Aschl, H., 1976. Versuche zum Verhalten von Beton unter mehrachsiger Beanspruchung. In München durchgeführtes Teilprojekt eines internationalen Vergleichsprogrammes. Versuchsbericht, Lehrstuhl für Massivbau, Technische Universität München.

Malvar, J.L., Crawford, J.E., Wesevich, J.W., Simons, D., 1997. A plasticity concrete material model for DYNA3D. International Journal of Impact Engineering 19 (9–10), 847–873.

Menétrey, Ph., 1994. Numerical analysis of punching failure in reinforced concrete structures. Ph.D. Thesis, Swiss Federal Institute of Technology, Lausanne, Switzerland.

Menétrey, Ph., Willam, K.J., 1995. Triaxial failure criterion for concrete and its generalization. ACI Structural Journal 92 (3), 311–318.

van Mier, J.G.M., 1986. Multiaxial strain softening of concrete. Part I: Fracture, materials and structures. RILEM 19 (111).

Mills, L.L., Zimmerman, R.M., 1970. Compressive strength of plain concrete under multiaxial loading conditions. ACI Journal, title no. 67-47, pp. 802–807.

Pivonka, P., Lackner, R., Mang, H.A., 2000. Numerical analyses of concrete subjected to triaxial compressive loading. European Congress on Computational Methods in Applied Sciences and Engineering, ECCOMAS 2000, Barcelona, 11–14 September 2000.

Scholz, U., Nechvatal, D., Aschl, H., Linse, D., Stöckl, S., Grasser, E., Kupfer, H., 1995. Versuche zum Verhalten von Beton unter dreiachsiger Kurzeitbeanspruchung. Deutscher Ausschuss fur Stahlbeton, Heft 447, Berlin, 64pp.

Simo, J.C., Ortiz, M., 1985. A unified approach to finite deformation elasto-plastic analysis based on the use of hyperelastic constitutive equations. Computer Methods in Applied Mechanics and Engineering 49, 221–245.

Simo, J.C., Taylor, R.L., 1985. Consistent tangent operators for rate-independent elasto-plasticity. Computer Methods in Applied Mechanics and Engineering 48, 101–118.

Smith, S.H., 1985. On fundamental aspects of concrete behavior. M.Sc. Thesis, Department of Civil Engineering, University of Colorado, USA, 192pp.

Zeng, L.F., Horrigmoe, G., Andersen, R., 1996. Numerical implementation of constitutive integration for rate-independent elastoplasticity. Computational Mechanics 18, 387–396.